

Effect of laser power on the microstructure and mechanical properties of laser-assisted cold sprayed 7075 aluminum alloy deposits

Kang Wang ^{a,b}, Lijia Zhao ^{a,b}, Tianliang Mao ^a, Xinyu Cui ^a, Jiqiang Wang ^{a,*}, Tianying Xiong ^a

^a Shi-changxu Innovation Center for Advanced Materials, Institute of Metal Research, Chinese Academy of Science, Shenyang 110016, PR China

^b School of Materials Science and Engineering, University of Science and Technology of China, Shenyang 110016, China



ARTICLE INFO

Keywords:

Laser-assisted cold spray
7075 alloy
Microstructure evolution
Mechanical properties
Strengthening mechanisms

ABSTRACT

7075 aluminum alloy deposits were fabricated using a solid-state additive manufacturing (AM) technology called laser-assisted cold spray (LACS). The effect of laser power on the microstructure evolution and mechanical property in the LACSe 7075 deposits was investigated. The microstructure of all deposits was analyzed by optical microscopy (OM), X-ray diffraction (XRD), and scanning electron microscopy (SEM) attached with energy dispersive spectroscopy (EDS) and electron backscatter diffraction (EBSD) systems. Pull-off adhesion, microhardness, and tensile tests were performed to assess their mechanical behaviors. The deposits showed a virtually linear increase in thickness with increased laser power and a minimum porosity of about 0.2%. With the accelerated diffusion of solute elements in deposits, lamellar η phase – Mg(Zn, Cu, Al)₂ and Al₇Cu₂Fe precipitated along grain boundaries at 2.6 kW eventually. Meanwhile, significant grain growth and recrystallization were initiated at the severely deformed prior-particle interfaces. All the LACSe deposits exhibited a noticeable increase in adhesion strength and a slight decrease in microhardness compared to the CSed one. The ultimate tensile strength (UTS) and elongation to fracture (EL) were improved by up to ~46% and ~35% in LACSe 7075 deposits. The relationship between mechanical properties and microstructure and the contribution of underlying strengthening mechanisms involved in the LACS process were then thoroughly discussed.

1. Introduction

7075-T6 aluminum alloy has been extensively employed as a structural material in both civil and military aircraft owing to its superior strength, machinability, and relatively low cost [1]. Recently, additive manufacturing (AM) has emerged in the aerospace industry as a promising technology when we consider its benefits including significant cost and lead-time reductions, a high degree of customization in design and materials, and consolidation of multiple components for performance enhancement, e.g. [2]. But some problems remained in selective laser melting (SLM) and wire and arc additive manufacturing (WAAM) - the most widely studied fusion-based AM methods of 7075 alloy currently. First, Zn and Mg are both low-boiling-point solute elements in 7075 alloy. They tend to vaporize when the raw powder is melted, which leads to a compositional deviation from the standard value [3,4]. For instance, Kaufmann et al. reported up to 30.8% weight loss of the primary strengthening constituent Zn in the SLSe 7075 alloy, which in turn reduced its mechanical properties [5]. Worse yet, 7075 alloy presents a broader solidification temperature range than the print-friendly Al-Si

alloys. Large amounts of primary solid phases form during solidification, which lowers the fluidity of liquid phases and causes shrinkage and bad metallurgical bonding in it [6]. Furthermore, it has been frequently reported that severe hot cracks inclined to develop in the intercolumnar region, which progressed along the building direction under the effect of residual stresses resulting from the thermal gradient during the additive process [5,7]. The appearance of hot cracks and microstructural anisotropy inevitably degrades the mechanical performance of SLSe 7075 alloy, particularly when the cracks cannot be eliminated by process parameters optimization. Considering the inherent shortcomings of fusion-based AM technology, other AM method for 7075 alloy still needs to be explored.

Recently, Cold Spray (CS) has been recognized as a potential AM technology to fabricate and restore various metal components [8]. Cold spray is a solid-state process where micro-sized metal powders are accelerated by a high-velocity gas jet and deposited on a substrate as a result of severe plastic deformation [9]. Less deleterious effects like oxidation, phase transformation, decomposition, and grain growth are triggered due to its relatively low work temperature compared with the

* Corresponding author.

E-mail address: jqwang11s@imr.ac.cn (J. Wang).

SLS process. However, CSed metal materials generally lack plasticity owing to the severe plastic deformation of particles during deposition. The layered structure with widely-distributed non-bonded interfaces between particles shown in its fracture surfaces, and became the predominant limitation for mechanical performance improvement in CSed 7075 alloy [10]. Meanwhile, the propulsive gas must supply powders with sufficient kinetic energy when depositing strong materials like 7075 alloy by increasing gas temperature and pressure or replacing air with helium, which would increase the risk of nozzle fouling and cost at the same time.

Under these circumstances, Bray et al. proposed a new strategy to increase deposition efficiency and improve mechanical properties by combining the advantages of laser and cold spray simultaneously [11]. The laser is used to heat the deposition site to between 30% and 80% of its melting point, which reduces the particle strength and enables them to deform at a much lower impact velocity [12]. Those high-strength materials which cannot be deposited with CS, such as tungsten [13], Ni60 [14], Stellite 6 [15–17], and metal metrics composites like WC/SS316L [18], diamond/Ni60 [19], WC/Stellite 6 [20], diamond/Cu [21] have been succeeded in obtaining oxide-free and dense deposits with the aid of the new technology called Laser-Assisted Cold Spray (LACS). According to the research of Birt et al. [22], three independent thermal parameters (ITPs) – laser power, mass flow rate, and velocity of workpiece motion, which are relatively unlinked to the particle velocity or ‘mechanical’ portion of the thermomechanical processing, play an important part in the formation of final deposits microstructure. The laser power is one of the key ingredients that directly determines the overall heat input during the process. Olakanmi et al. has done some basic investigation on the deposition mechanism and microstructure of LACSD Al-12Si alloy and optimization of LACSD pure Al deposit with different laser power [23,24]. The deposits showed a much better bonding between particles with significantly increasing deposition efficiency under appropriate laser power. However, no studies have been conducted on the parameter optimization and mechanical properties test of LACSD high-strength 7075 aluminum alloys up to now.

Anyway, the LACS AM method is expected to effectively mitigate the hot cracks produced in the SLSed 7075 alloy as well as improve the mechanical properties of the LACSD deposits in comparison to the CSed deposits. Moreover, it’s of great application value to investigate the microstructural control of LACS through the in-situ laser heat treatment to the entire deposits, which will be beneficial for the ideal mechanical property acquisition in the large restoration parts that are not convenient for reheat treatment. Therefore, This paper aims to expand on the effect of in-situ laser heating on the microstructure evolution and mechanical properties change of CSed 7075 alloy with a specific focus on the following issues: 1) generation, development, and influences of macroscopic defects in the LACS process, 2) microstructure evolution of LACSD deposits, including compositional separation, precipitates, and grain information, and 3) mechanical properties evaluation and the underlying strengthening mechanisms with microstructure evolution.

2. Materials and methods

2.1. Materials

A commercial gas-atomized 7075 Al alloy powder with a nearly spherical shape was supplied by Yuanyang Technology Ltd. in Henan province of China. The nominal chemical composition of the 7075 powder was detected as 90.2 wt%Al–5.1 wt%Zn–2.6 wt%Mg–1.6 wt% Cu. It was deposited on a 7075-T6 plate with a dimension of 40 × 30 × 5 mm³. Before powder spraying, the surfaces of substrates were blasted with 120 mesh Al₂O₃ grit and then ultrasonically cleaned with alcohol to improve the adhesion of deposits to them.

2.2. LACS equipment and parameters

The schematic diagram of the LACS additive manufacturing system is shown in Fig. 1. The LACS equipment used in this study included a 4 kW diode laser system of 976 μm wavelength and a homemade cold spray device equipped with a De-Laval cylindrical WC nozzle. The laser system was mounted to the mechanical arm at an angle of 30° to the substrate surface normal. It proceeded with the nozzle and irradiated the area where the powder jet collided with substrates. The laser spot was 4 mm in diameter and kept underneath the nozzle during the spray process. The laser power varied from 1.8 kW to 2.6 kW at an interval of 0.4 kW. In the subsequent paragraph, L0, L1, L2, and L3 were used in turn referring to the CSed deposits and LACSD deposits fabricated with laser power of 1.8 kW, 2.2 kW, and 2.6 kW for convenience narration. Compressed air was used as the propulsive gas, and the temperature and pressure during the deposition were maintained at 250 ± 10 °C and 3.0 ± 0.2 MPa, respectively. The powder feeding rate was regulated at a fixed value of 25 g/min, and the stand-off distance was kept at 30 mm during the whole depositing process. The laser traveled along a zigzag-shaped scanning path traveled at a pace of 50 mm per second. Ten layers of LACSD 7075 alloy deposits were created at each laser power for further research.

2.3. Materials characterization

A 10 × 10 × 5 mm³ cubic specimen for microstructure characterization was cut from the center of each deposit using a wire-cut electrical discharge machine. These specimens were grounded with sandpaper to 2000 grit, mechanically polished to a mirror surface with 0.08 μm silicon dioxide polishing fluid, and then followed by ultrasonic cleaning in alcohol. The deposits were etched with Keller’s reagent for 1 min before being examined under a light optical microscope (Nexcope, NM910, China) to properly observe the bonding state of the deposit-substrate interface and particle deformation.

The phase in the deposits was identified by X-ray diffraction (SmartLab, Rigaku Corporation, Japan) with Cu Kα monochromatic radiation in the range of 2θ = 10–90° and a step size of 0.05°. The average grain diameter, *d*, and microstrain, *ε*, of each sample used to calculate the dislocation density in CSed deposits and LACSD deposits were obtained according to the Williamson-Hall Eq. (1) [25]:

$$B \cos \theta_B = \frac{K\lambda}{d} + \epsilon \sin \theta_B, \quad (1)$$

where *B* is the peak broadening term, *λ* is the wavelength of Cu Kα₁ radiation, i.e. 1.54 Å, *K* is ~0.9, *d* and *ε* were calculated from the slope and intercept of the linear regression line of the *B*cosθ_B vs *ε*sinθ_B curve. The peak broadening *B* is obtained from the measured full width at half-maximum (FWHM) values after subtracting the instrumental broadening value as Eq. (2) described:

$$\sqrt{B_{obs}^2 - B_{inst}^2}, \quad (2)$$

where *B_{obs}* is the observed peak broadening, and *B_{inst}* is the instrumental broadening.

The variations in constituent and grain for all the specimens were evaluated by an SEM (Apreo 2, FEI, United States) attached with energy dispersive X-ray (EDX) and EBSD systems. Software (Fiji) for image analysis was used to determine the porosity and thickness of the deposition in each sample, and at least 10 cross-sectional pictures taken at a magnification of 500 were chosen to assure accuracy.

2.4. Mechanical properties evaluation

Measurements of Vickers microhardness were conducted on the as-polished cross-section of the deposits using a Vickers microhardness

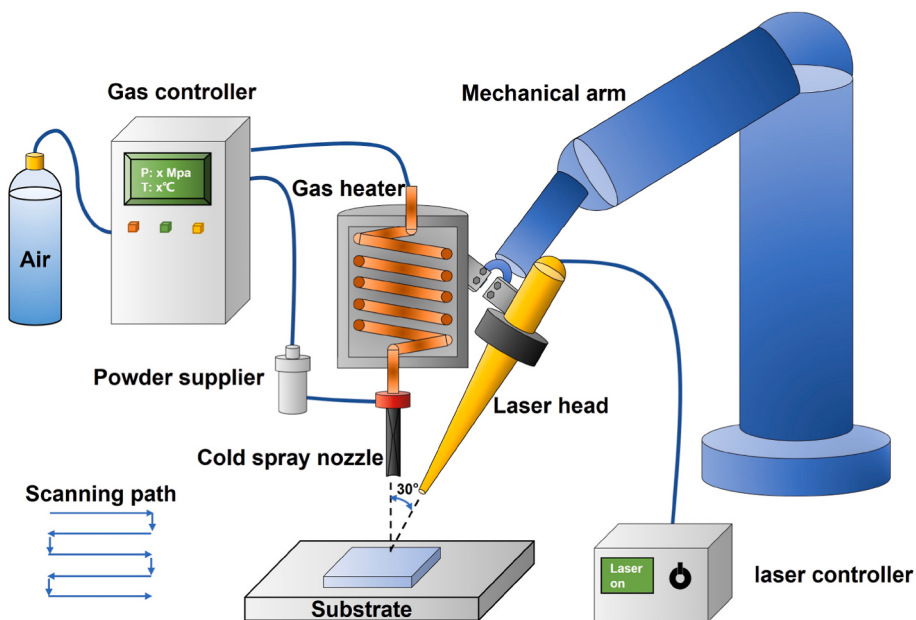


Fig. 1. Schematic diagram of LACS additive manufacturing system.

test machine (YMVS-1, MEGA instruments, China). The specimens were subjected to a 50-g load for 15 s, and at least 20 measurements were made for each deposit as per ASTM-E384-17. Pull-off tests following ASTM C633 were performed on a universal tensile test machine (AG-100KN, Shimadzu, Japan) with a constant tensile speed of 0.5 mm/min to assess the deposit-substrate adhesion strength. The deposits, together with the substrate, were cut into 25 mm-diameter cylinders and were ultrasonically cleaned in alcohol for 10 min to remove the grease. Then the specimens and the pull-off test grips were attached on both sides using an E-7 epoxy adhesive (Shanghai Research Institute of Synthetic Resins, China) and kept at 170 °C for 4 h under pressure to solidify.

Three different specimens were prepared for each laser power to ensure repeatability. Dog-bone-shaped specimens for tensile tests were wire-cut machined with a gauge dimension of $\sim 5 \times 1 \times 1$ mm³. The tensile samples ended up grinding with 2000 grit sandpaper and ultrasonic cleaning in alcohol. The tensile tests were performed at room temperature using a universal testing machine (Z100, Zwick/Roell, Germany) with strain measured by a laser extensometer. The strain rate was set at 0.5 mm/min. Four samples for each condition were tested to ensure repeatability.

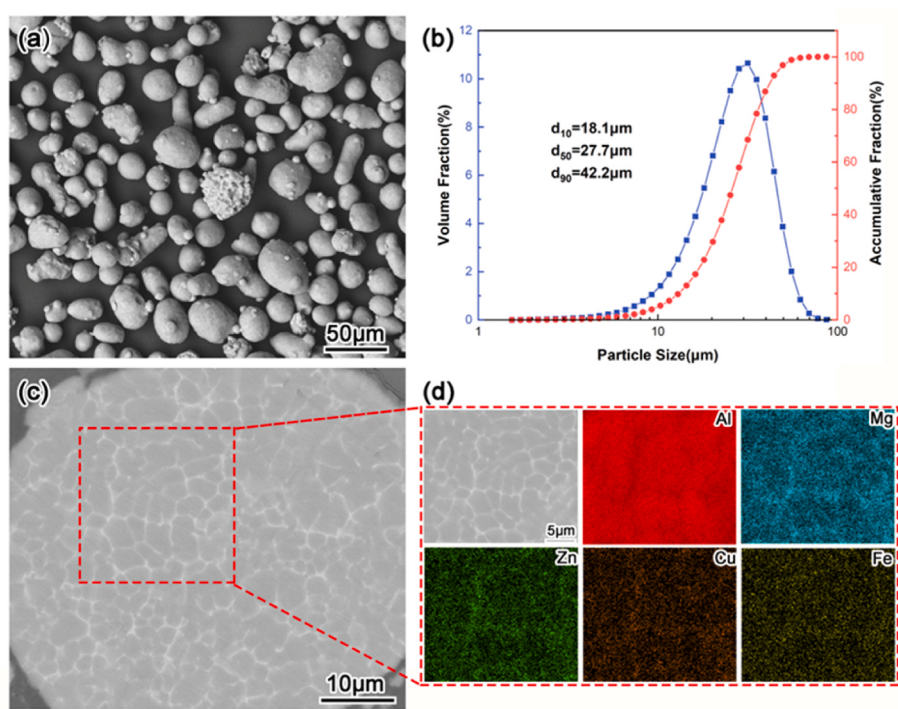


Fig. 2. Analysis of the as-received 7075 alloy powder, (a) SE image of overall morphology, (b) particle size distribution diagram, (c) BSE image of particle's cross-section, (d) EDS mapping on the magnified view showing the solute elements distribution.

3. Results

3.1. Feedstock powder

Fig. 2(a) shows the overall morphology of the as-received 7075 alloy powder. The majority of them were globose with only a few cylinder-shaped particles. **Fig. 2** depicts a log-normal particle size distribution and d10, d50, and d90 of the powder are respectively measured at 18.1, 27.7, and 42.2 μm . **Fig. 2(c)** displays a near-equiaxed grain structure with grains of several microns in diameter in the cross-section of 7075 particles. Meanwhile, apparent composition segregation is observed at the grain boundaries and the EDS mapping results of the magnified view in **Fig. 2(d)** show that the solute elements of Zn, Mg, Cu, and Fe in 7075 alloy are enriched here. Some reasons may be responsible for the strong composition varying, including high solidification and cooling rate, pre-solidified microdroplets and dendrite fragments, as well as thermal equilibration and partial re-melting of solid particles [26]. The microhardness of the particles was measured about 101 Hv on average through a Vickers microhardness tester.

3.2. Influence of laser power on deposition thickness and quality

Fig. 3(a)–(d) depicts the optical images on the etched cross-section of CSed and LACSe deposits. The same weight of 7075 powder approximately 200 g was sprayed in 10 passes for each parameter to compare their deposition efficiency. The L2 deposits show fewer defects, including pores, detachments, and non-bonded interfaces. The pores in L0, L1, and L2 deposits are mainly located at the interparticle junction of the deformed particles with sizes varying from a few microns to tens of microns. More pores were scattered at the upper layers in the three deposits due to the weakening of the peening effect of successive particles. The number of pores greatly increased in the L3 deposits, and the pores were widespread in the upper layers as shown in **Fig. 3(d)**. The formation of these pores is believed to be attributed to surface oxidation and it will be discussed in detail in the latter section. No obvious detachments between the particle-substrate and interparticle interfaces were observed in all three LACSe deposits, indicating enhanced adhesive and cohesive properties compared with the CSed one. In addition, the progressive disappearance of the non-bonded interfaces between particles also served as strong proof of the improvement in bonding

conditions. As laser power increased, the overlaid particle morphology was finally replaced by the well-bonded, bulk-material-like morphology. It may be reasonable to infer a transformation of the primary bonding mechanism in LACSe 7075 deposits, which should be responsible for its mechanical properties change.

Fig. 4 illustrates the variation of deposition thickness and porosity of the deposits with the increased laser power. The deposition thickness raised almost linearly and peaked at 1.2 mm in L3 deposits. This figure is about five times greater than the CSed L1 deposits fabricated under identical process parameters. The minimum porosity of roughly 0.1% was gained in the L2 deposits, which is over 20 times lower than the porosity of the CSed L1 deposits. The improvement of laser on the thickness and quality of 7075 deposits is realized by affecting the particle impact conditions directly -i.e., particle impact velocity and particle impact temperature as other high-quality CS processes had done. Sabard et al. [27] made excellent 7075 CSed deposits with porosity as low as 0.3% using N₂ as carrier gas under 5 MPa gas pressure and 500 °C gas temperature. Although the air was selected as carrier gas and a much

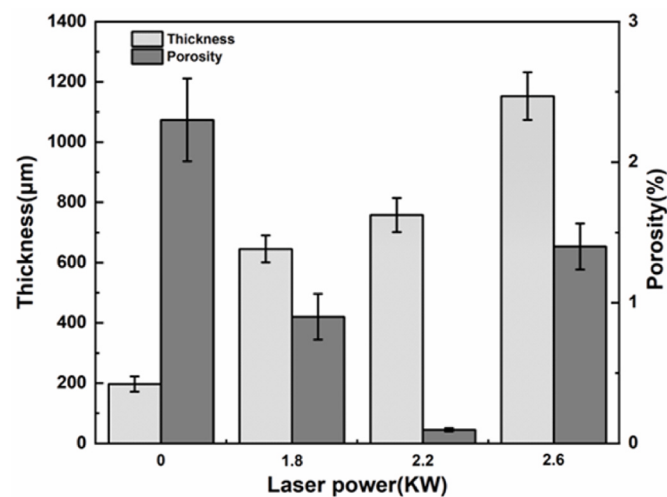


Fig. 4. Histogram of deposition thickness and porosity of CSed and LACSe 7075 deposits.

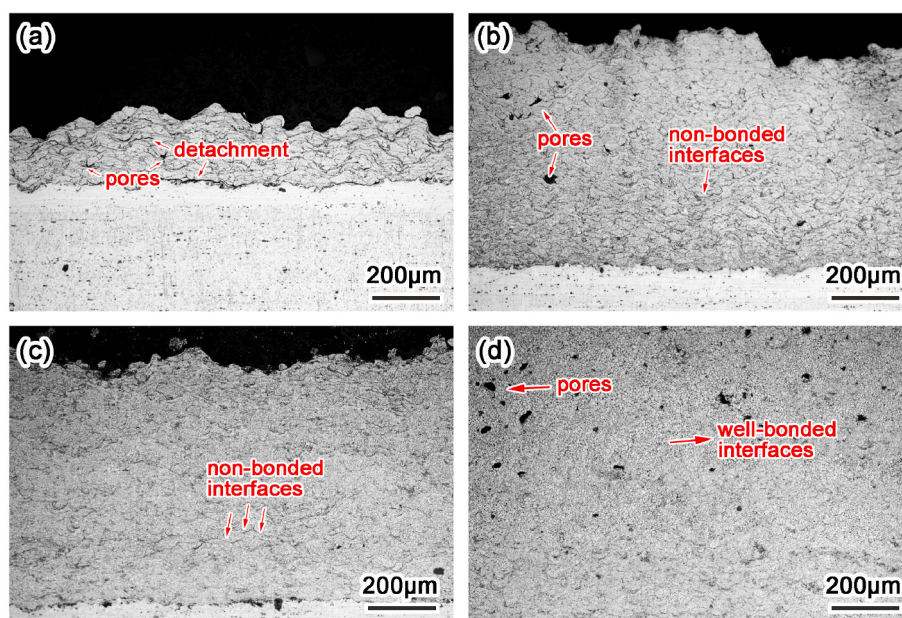


Fig. 3. Optical images on the etched cross-section of (a) L0 deposits, (b) L1 deposits, (c) L2 deposits, (d) and L3 deposits.

lower process parameter was adopted in this study, deposits with equivalent quality deposits were finally obtained with the assistance of the laser.

3.3. Microstructure evolution with laser power

3.3.1. Solute element diffusion and second phase precipitation

Fig. 5 shows the BSE images of the cross-section microstructure of the CSed 7075 deposit and LACsed 7075 deposits. The accelerated diffusion of solute elements with increased laser power is a noteworthy feature in LACsed 7075 deposits. Fig. 5(a-d) depicts a typical dendritic structure as the gas-atomized powder, which implied the composition separation is preserved in the L1 and L2 deposits. It demonstrated that the heat input introduced during the process is too low to activate the diffusion of solute elements. The enhanced diffusion trend, which was corroborated by the attenuation of contrast in grain boundaries in the L3 deposits,

resulted in the obtainment of a more uniform 7075 material. Fig. 5(g-h) exhibits that fine and lamellar precipitates developed along the grain boundaries forming a network structure with some intermetallic particles found inside the Al grains in L3 deposits as laser power continues to increase. The composition of this intermetallic was identified as follows. Many micropores were found located at the grain boundaries as well.

The primary intermetallic phases during solidification of as-cast Al-Zn-Mg-Cu alloy were demonstrated by numerous investigations to be $\eta(\text{MgZn}_2)$, $T(\text{Al}_2\text{Mg}_3\text{Zn}_3)$, $S(\text{Al}_2\text{CuMg})$, and $\theta(\text{Al}_2\text{Cu})$ and so on [28–30]. XRD and SEM-EDS characterization was carried out to identify the exact phases generated during the LACS process. Fig. 6 illustrates the XRD pattern of the as-received 7075 powder along with the CSed and LACsed deposits. Apart from the FCC crystalline structure Al phase, the peaks of T phase - $\text{Mg}_{32}(\text{Zn}, \text{Cu}, \text{Al})_{49}$ that represented by the solid circle were present in the as-received 7075 powder. The T phase was maybe the grid-like white phase at the grain boundaries shown in Fig. 2 (c),

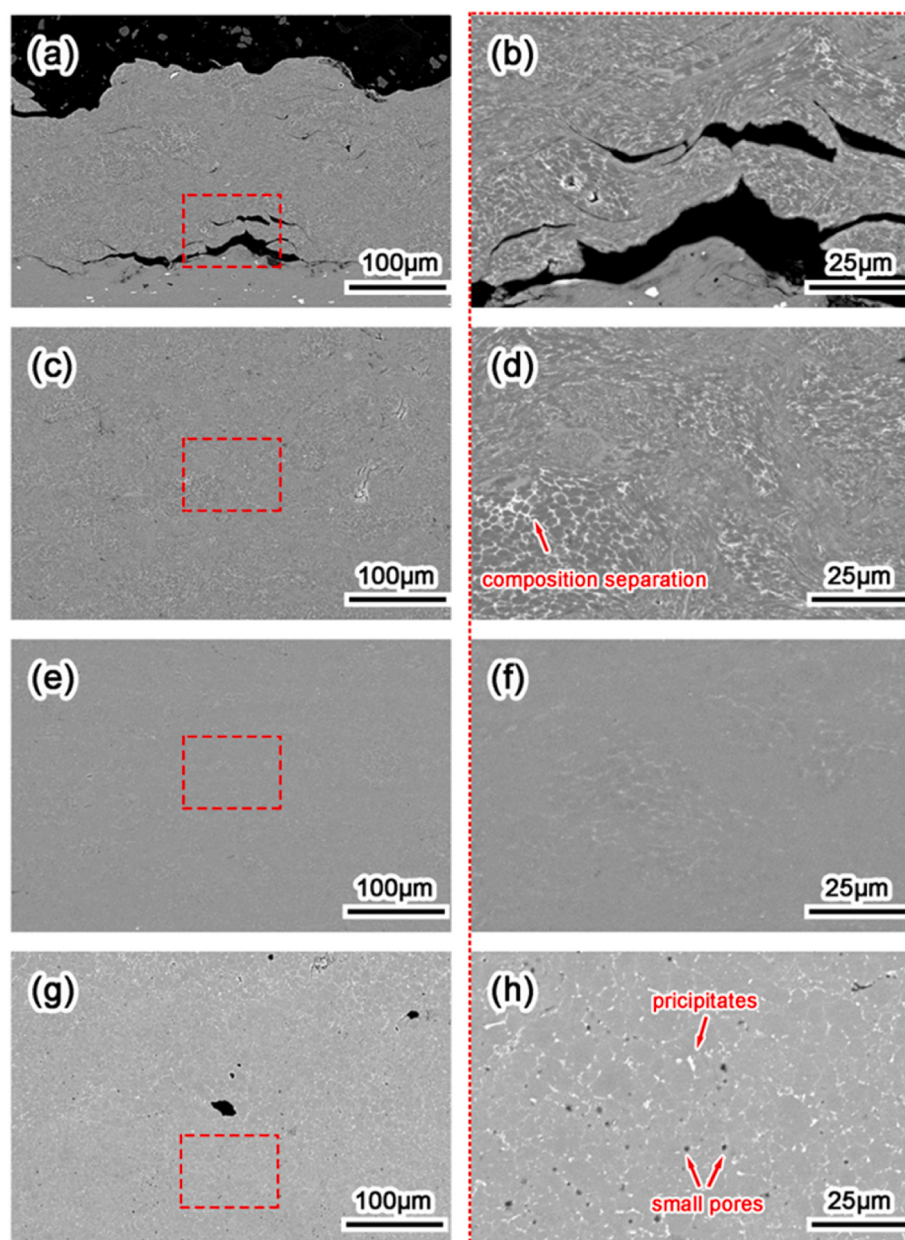


Fig. 5. BSE images show the cross-section microstructure of (a-b) L0 deposits, (c-d) L1 deposits, (e-f) L2 deposits, and (g-h) L3 deposits. Images on the right column are the zoom-in picture of the areas encircled by the red boxes on the left column. (For interpretation of the references to color in this figure legend, the reader is referred to the Web version of this article.)

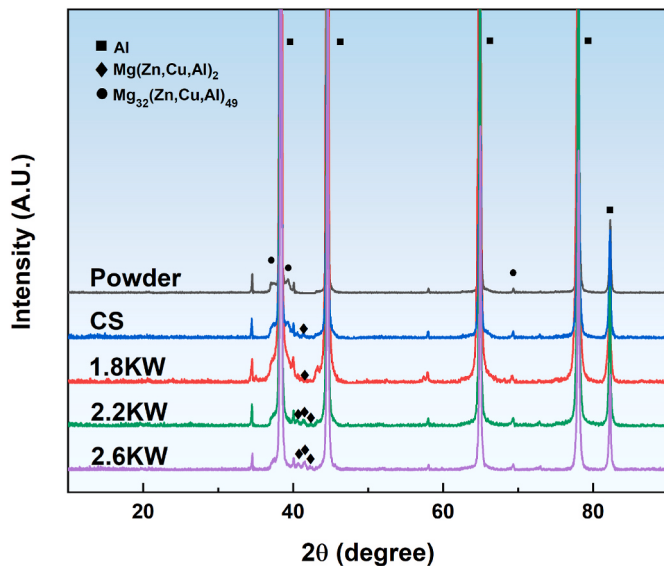


Fig. 6. XRD pattern of as-received powder, CSed deposits, and LACSed deposits.

which typically occurs during the rapid solidification process in the atomization and was extensively documented in the gas-atomized 7075 powder [31–33]. Then, the CSed deposit and LACSed deposits form a new strengthening phase, η -Mg(Zn, Cu, Al)₂ as laser power increased, which is fairly common in CSed 7075 depositions [26] and AM 7075 materials by SLM or WAAM [34–36]. Meanwhile, the XRD pattern exhibits a reduction of the T phase and an elevation of the η phase with the increased laser power.

The BSE images and corresponding EDS analyses of the LACSed L3 deposits are shown in Fig. 7. According to the EDS mapping results, these intermetallic compounds were enriched in Zn/Cu/Mg/Fe. Besides the η phase that showed a high content of Mg and Zn like P3 and P4, another phase enriched in Cu and Fe was also found along the grain boundary as the yellowish arrows pointed to in Fig. 7. The composition of these phases was listed in Table 1. The phase in P1 and P2 can be deduced as Al₇Cu₂Fe considering the relatively higher content of Fe and Cu compared with P3 and P4, which has been reported in the WAAM

Table 1

The composition (wt %) of points marked in Fig. 7

	Mg	Cu	Zn	Fe	Cr	Al
P1	2.7	2.8	5.8	5.9	0.4	Bal.
P2	2.2	2.3	5.9	3.3	0.3	Bal.
P3	4.4	4.7	9.2	0.6	0.1	Bal.
P4	4.8	3.2	7.3	2.9	0.3	Bal.

7075 alloy as well [35]. Certainly, the determination of the phase was still largely speculative, and more convincing evidence like TEM results should be adopted to verify it.

3.3.2. Grain morphology, size, and recrystallization

The change of grain structure, including grain size, morphology, and boundaries based on EBSD analysis, is presented in Fig. 8. Fig. 8(a)–(d) shows the IPFs of L0, L1, L2, and L3 deposits, respectively. Fig. 8(a) shows that the inhomogeneous plastic deformation took place in CSed 7075 particles. Heavier deformation and grain refinement occurred at the periphery of particles when compared with the interior regions. The residual stress caused by the high-velocity impact of particles was concentrated that no indexing was found here. The microstructure here may experience recrystallization and marked grain refinement down to the nanoscale, which has been proved to be induced by adiabatic shear instability (ASI) at a high strain-rate deposition process by previous studies [37–39]. A noticeable increase in average Al grain size from 0.63 μ m to 2.33 μ m with rising laser intensity was observed and illustrated in Fig. 8(e–h). The L1 and L2 deposits shown in Fig. 8(b) and (c) maintained a similar microstructure (i.e., elongated grains and high-stress regions) to the CSed L0 deposits despite a slight grain growth and merging over the entire cross-section. The L3 deposits shown in Fig. 8(d) presented a radical transition to fully recrystallized equiaxed grains showing a perfect combination between particles. The grain growth and non-bonded interface disappearance shown in Fig. 8(d) were probably due to the onset of dynamic recrystallization (DRX) and the residual stress relief under the ‘annealing’ effect of laser. The random distribution of IPF colors in Fig. 8(a–d) also indicates no preferred crystallographic orientation within the patterned regions of deposits.

Fig. 9(a–d) displays the boundary and band contrast maps of the CSed and LACSed 7075 deposits. The red line and blue line represented low-angle grain boundaries (LAGBs) with a misorientation angle between 2° and 15° and high-angle grain boundaries (HAGBs) with a

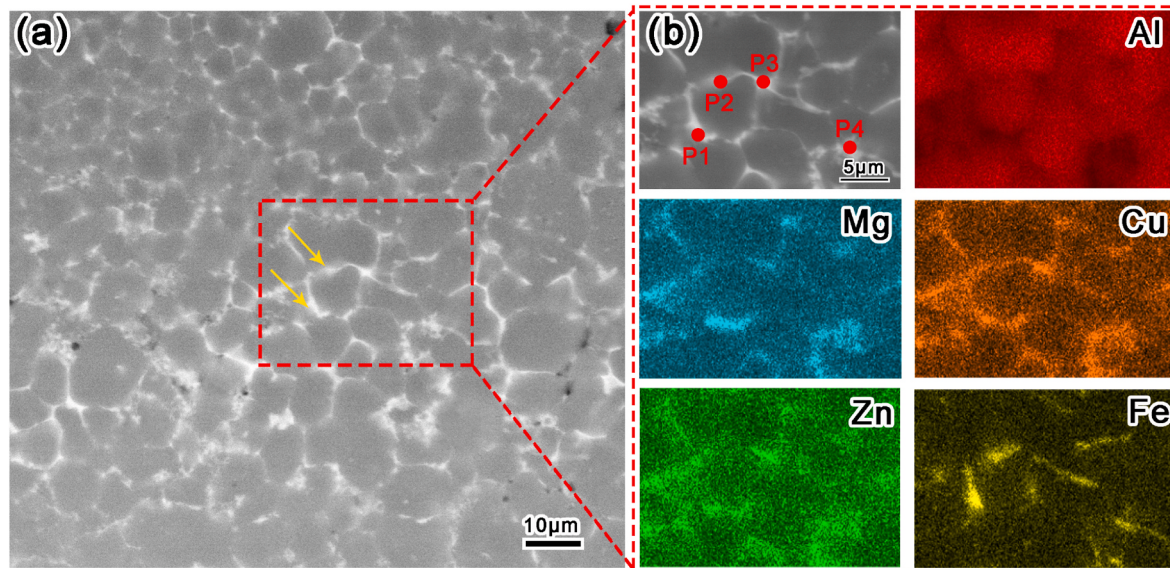


Fig. 7. BSE images showing the grid-like precipitates in LACSed deposit in L3 deposits, (a) the overview of the deposit with yellowish arrows pointing to Cu, Fe enriched areas, (b) EDS mapping of the magnified region in (a).

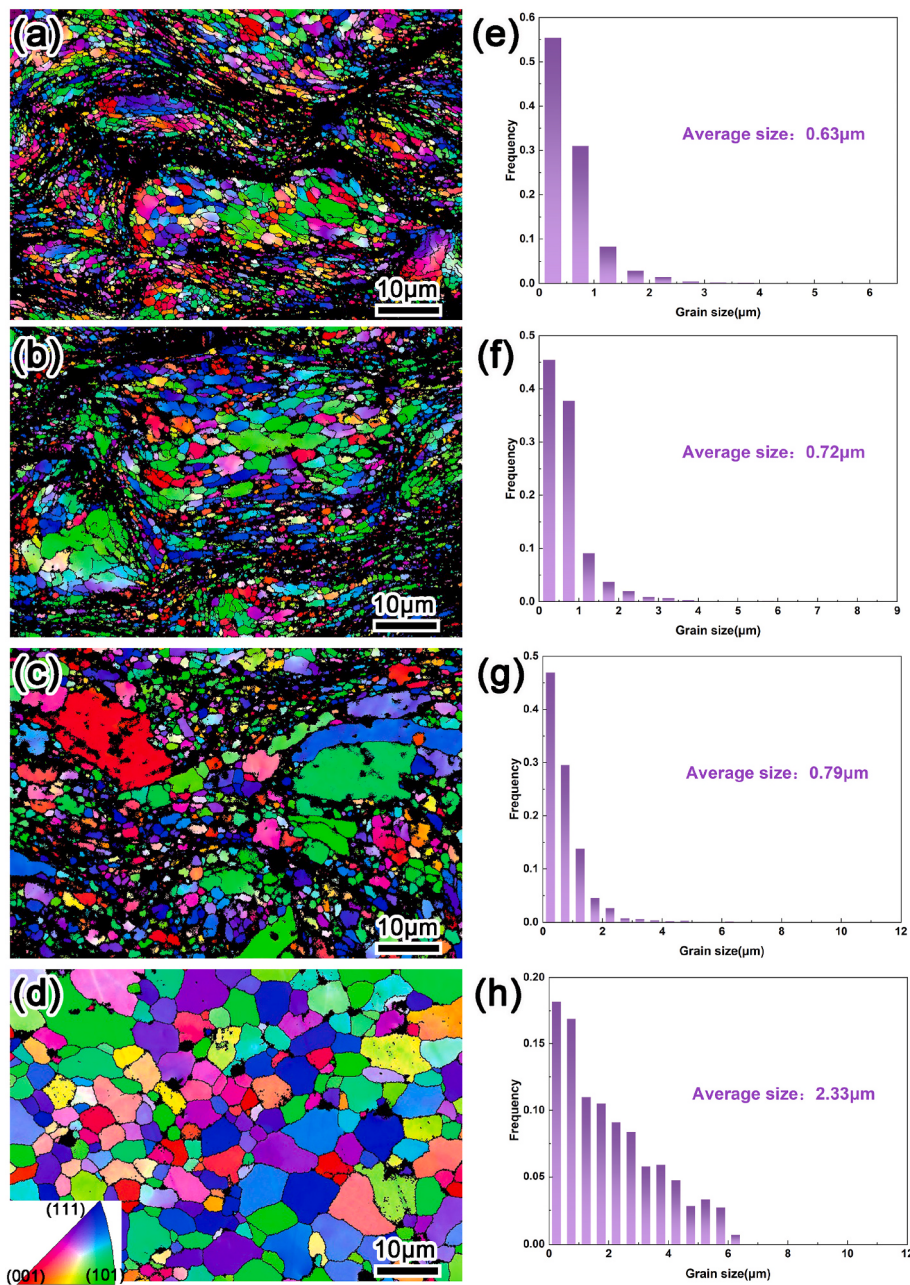


Fig. 8. EBSD images of CSed and LACSED 7075 deposits, (a–d) inverse pole figures (IPF) of L0, L1, L2, and L3 deposits, respectively, (e–h) corresponding grain size distribution diagram.

misorientation greater than 15° , respectively. As reported, the LAGBs developed during deformation for materials with high stacking fault energy (SFE) will gradually evolve into HAGBs during the DRX process [40]. The fraction of HAGBs significantly increased from 0.049 to 0.315 with the rising laser power, which implied the occurrence of DRX. The increase in the proportion of DRXed grains can be visualized through the grain orientation spread (GOS) map shown in Fig. 9(e–h) as well. The average GOS value for a set of I grains is defined as

$$GOS(i) = \left(\frac{1}{I} \right) \sum_i \left[\frac{1}{J(i)} \sum_j \omega_{ij} \right], \quad (3)$$

where $J(i)$ is the number of pixels of grain i and ω_{ij} the misorientation angle between the orientation of pixel j and the mean orientation of grain i [41]. The GOS value is associated with macroscale plastic deformation in materials. A higher GOS value is usually caused by the

distortion of grains, indicating a greater degree of plastic deformation here. In Fig. 9(e–h), the blue, yellow, and red regions represented DRXed grains, recovered, and deformed grains with GOS values less than 2° , between 2° and 7.5° , and higher than 7.5° , respectively. Compared with the CSed deposits, the area proportion of DRXed grains in the L3 deposits rose from 14.7% sample to 32.9%, whereas that of deformed grains fell from 29.5% to 0.9%. This result coincided well with the former progressive increase in the proportion of HAGBs with rising laser intensity.

The KAM maps, which correlate well with the plastic strain in polycrystal materials, were plotted to quantitatively assess the degree of plastic deformation in deposits. Fig. 10 shows the rainbow scale KAM maps of CSed and LACSED deposits with their corresponding statistic histogram. KAM is defined as the arithmetic mean of the scalar misorientation between groups of pixels or kernels [42]. Fig. 10(a–d) demonstrates that the high KAM zones greatly overlapped with the LAGBs with them located within the grains and forming a network structure.

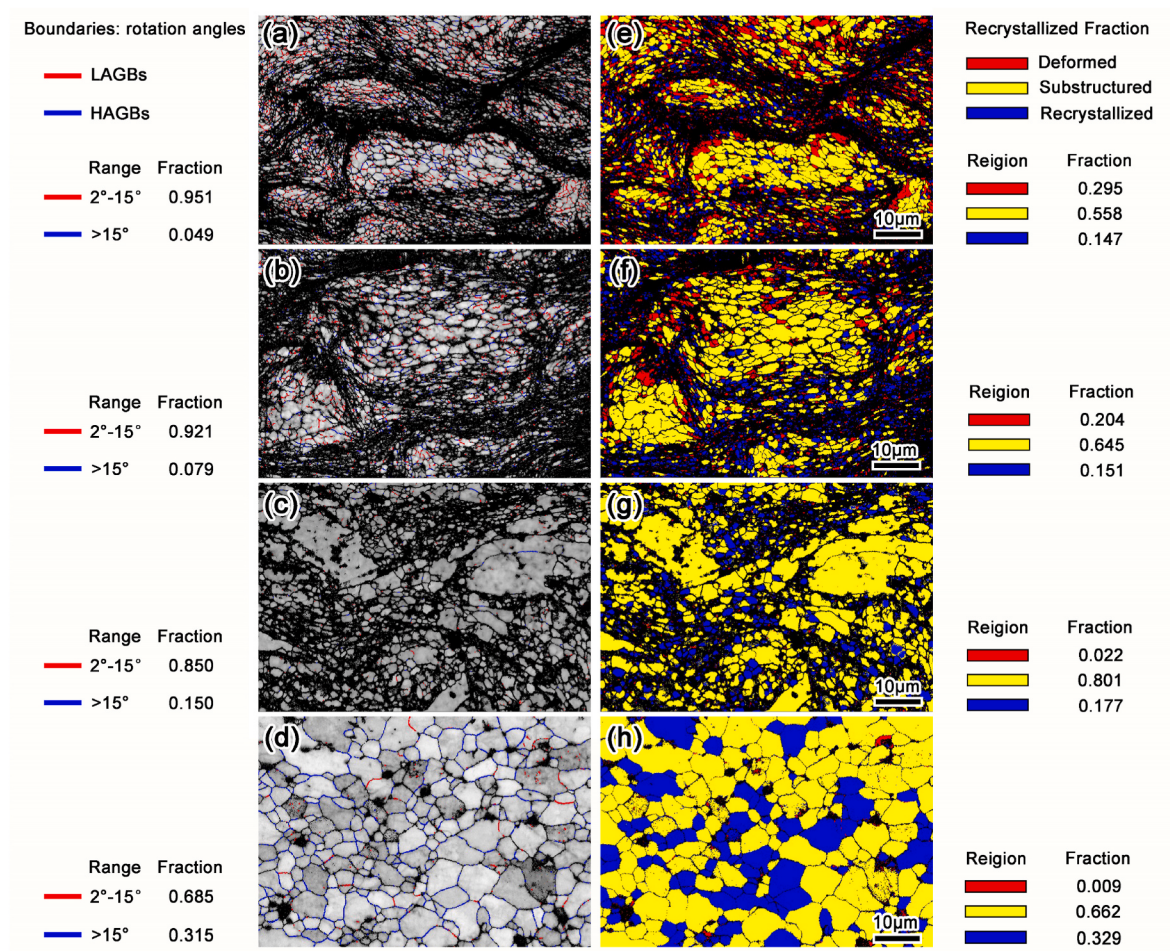


Fig. 9. DRX behavior of L0, L1, L2, and L3 deposits, (a-d) grain boundary maps showing the LAGBs and HAGBs with their respective proportions, (e-h) GOS maps showing the classification of recrystallized, recovered, and deformed grains with their respective proportions.

The network structure vanished progressively as the laser intensity rose and high KAM zones began to spread around the pores. Fig. 10(e-h) exhibits the histogram of KAM angle distribution and the average KAM angle decreased from 0.628° to 0.342° . The lowering KAM angle suggested an alleviation in localized strain and a reduction in defects like dislocation density under the ‘annealing’ effect of laser.

3.4. Adhesion strength and hardness measurements

The adhesion strength of the CSed deposits was approximately 22.8 MPa, which was significantly lower than that of the LACsed deposits. No precise adhesive strength of the LACsed deposits was eventually ascertained since it exceeds epoxy glue’s cohesive strength, which is less than 60 MPa (see Table 2). The adhesive strength at least doubled in LACsed deposits in contrast to that of the CSed ones. The disparity in measured values may originate from the elimination of obvious defects between the substrates and deposits to a large extent. The transformation of the primary bonding mechanism from mechanical interlocking to metallurgy bonding may also play a crucial role during the process.

Fig. 11 illustrates that the microhardness of the 7075 deposits underwent a complex fluctuation as laser power rose. The CSed L0 deposits exhibited the highest average hardness of 143 Hv due to the effect of work hardening and grain refinement as we mentioned above. The L1 deposits had the lowest microhardness of 123 Hv. The microhardness reduction was probably a result of the stress release caused by laser heat input. Subsequently, the microhardness increased to a higher value of 130 Hv in the L2 deposits, which may largely own to the decrease in

porosity. The microhardness of the L3 deposits dropped down to 123 Hv and tended to have a wider hardness dispersion. It seemed appropriate in light of the combined impact of broad pore defects and strengthening phase precipitation despite the significant grain growth in the deposit.

3.5. Tension property and fracture analysis

The tensile properties of LACsed 7075 deposits were characterized via a quasi-static tension test. Fig. 12(a) depicts the engineering stress-strain curves of all three LACsed 7075 deposits. The LACsed L1 deposits achieved a yield stress (YS) of 376 ± 9 MPa, an ultimate tensile strength (UTS) of 437 ± 6 MPa, and an elongation to fracture (EL) of $5.4 \pm 0.4\%$. The L2 deposits exhibited similar mechanical properties with a YS of 377 ± 22 MPa, a UTS of 432 ± 23 MPa, and an EL of $5.2 \pm 1.2\%$. Nevertheless, the L3 deposits showed a dramatically decreased UTS and an EL of 208 ± 45 MPa and $2.8 \pm 0.4\%$, respectively. The curve of L1 and L2 deposits reveals a slight work hardening with a yield ratio of about 86%. On the contrary, the L3 deposits fractured before yield, which suggested the brittle fracture occurred in L3 deposits. The mechanical properties of CSed 7075 alloy are unavailable in our investigation because we cannot obtain the samples with sufficient size for the mechanical due to its low deposition efficiency under the given processing parameters. The former study on the CS of 7075 alloy proved that its UTS varied from 240 MPa to 400 MPa and its EL varied from 2.0% to 4.0% [10,43,44]. The relative data is summarized and displayed in Table 3.

Fig. 12(b) compares the mechanical properties of LACsed 7075

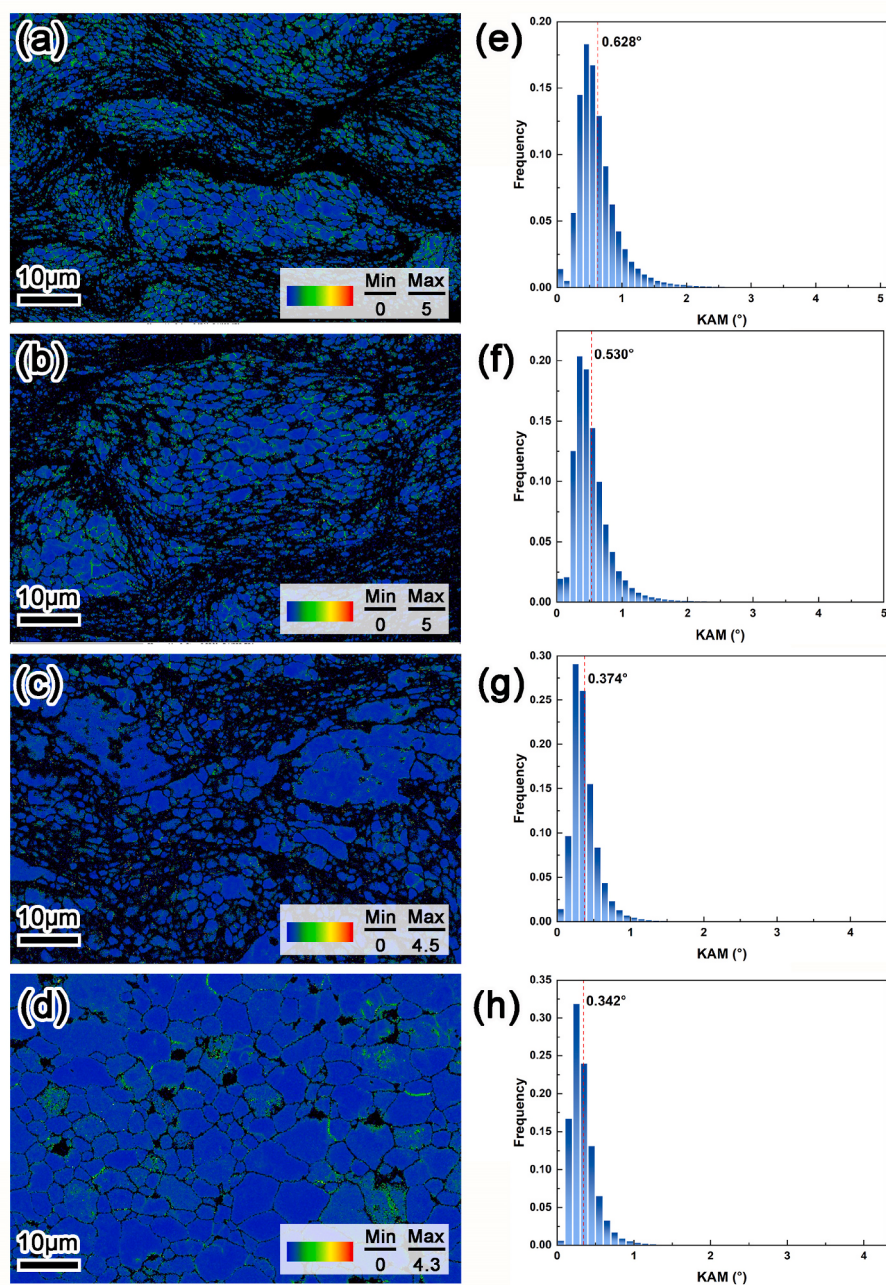


Fig. 10. EBSD KAM maps of (a–d) L0, L1, L2, and L3 deposits, respectively, and (e–h) histogram of KAM degree for each condition.

deposits with those Al–Zn–Mg–Cu alloys fabricated with WAAM [35, 45], SLM [6,36,46–50], CS [10,43,44] and conventional wrought 7075 alloys [51]. In this diagram, the solid symbols reflected the mechanical properties of Al–Zn–Mg–Cu alloys in their as-built condition, whereas the hollow symbols with the same color show their mechanical properties following a heat treatment (usually T6). The LACSeD sample showed a superior strength-ductility trade-off than most other Al–Zn–Mg–Cu alloys in the as-built state and close to the mechanical property of conventional wrought 7075 alloy. It is believed the LACSeD deposits will achieve a preferable tensile property for practical use after heat treatment.

Fig. 13 shows the fracture surface of the LACSeD 7075Al samples obtained under different laser powers. As shown in Fig. 13(a–b), the fracture surface of L1 deposits demonstrated typical layer morphologies with multiple cracks at interparticle interfaces [43]. Some dimples were located in the well-bonded interparticle regions, where heavier plastic

deformation and recovery occurred. In addition, the inter-splat failure between particles was also discovered. The non-bonded interface shown in Fig. 13(a–d) is a prominent feature in CSed deformable metallic materials. The contact zone between particles extends from the periphery to the center with increasing impact velocity but never covers the entire interface according to experiment and simulation results [52, 53]. This phenomenon is related to adiabatic shear instability (ASI), which occurs initially at the outer rim of the particle/substrate contact zone [9]. In the case of L2 deposits shown in Fig. 13(c–d), fracture took place almost in the same way as the L1 deposits along the particle interface. However, the fracture surface of L3 deposits displayed a predominant intergranular fracture along the network of intermetallic phases distributed along the boundaries of recrystallized grains as shown in Fig. 13(e–f). These lamellar intermetallic phases precipitated along the recrystallized grain boundaries are too hard and brittle to deform. This leads to crack initiation and facilitates the expansion of

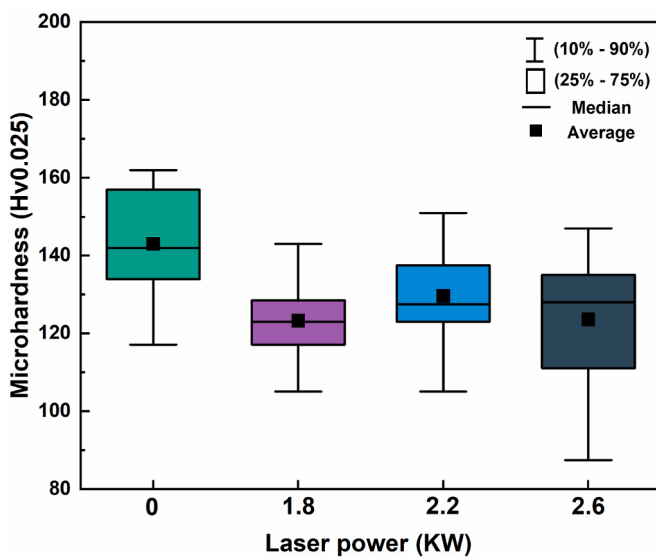


Fig. 11. The boxplot of measured microhardness of CSed and LACsed deposits at different laser power.

Table 2
Adhesion values of the CSed and LACsed deposits.

Sample	Adhesive strength (MPa)	Failure mode
CS	22.8 ± 3.4	Adhesive
LACS (1.8 kW)	Over 52.2	Glue failure
LACS (2.2 kW)	Over 55.3	Glue failure
LACS (2.6 kW)	Over 54.7	Glue failure

Table 3
Tensile properties of CSed sample and LACsed samples.

Sample	YS (MPa)	UTS (MPa)	EL (%)	Reference
CS	/	300	4.0	[43]
LACS (1.8 kW)	376 ± 9	437 ± 6	5.4 ± 0.4	This study
LACS (2.2 kW)	377 ± 22	432 ± 23	5.2 ± 1.2	
LACS (2.6 kW)	/	208 ± 45	2.8 ± 0.4	

intergranular cracks. Some dimples were found in the interparticle interfaces where intermetallic phases were not largely precipitated. Only a few non-bonded interfaces were found, showing that superior interparticle bonding occurred due to surface diffusion. Meanwhile, the

increased proportion of interior defects like pores within the deposits accelerated the failure during the tensile test and lowered the strength and elongation eventually.

4. Discussion

4.1. Possible strengthening mechanisms in the LACsed deposits

It is worth noting that the LACsed 7075 deposits in this study demonstrate better mechanical properties (high strength and low ductility) than the CSed deposits. It's valid to deduce the simultaneous improvement in strength and ductility is substantially related to the elimination of macroscopic defects, particularly the pores and non-bonded interfaces remaining between the particle splats. As for the variation of strength between the LACsed deposits, it may be attributed to the combining effect of grain-boundary strengthening, solid-solution strengthening, and dislocation strengthening. Their separate contributions to the strength are discussed in the following section.

4.1.1. Defects elimination

In the CS process, the bonding between particles occurs on the condition that the particle impact velocity (V_p) is beyond a critical particle impact velocity (V_{cr}). The cohesive strengths of deposited materials are a linear function of the parameter η , which is defined as the ratio of V_p to V_{cr} [54]. Typically, the parameter V_{cr} only relates to the intrinsic properties of powders, such as their types, sizes, surface oxidation conditions, and so on, whereas the parameter V_p is affected by process parameters on gas, nozzle, procedure, and so forth [9]. Consequently, adjusting the process parameter to increase the V_p is a practical approach for enhancing the mechanical performance of CSed materials.

However, it is essential to point out that the bonding extends from the periphery to the center of the inter-particle interface but never encompasses whole splats with rising V_p , which results in the generation of a large number of non-bonded interfaces that severely limit the mechanical properties enhancement of CSed materials. In the LAC process, the non-bonded interfaces progressively diminished as laser power increased. The inter-particle interfaces in the recrystallized region of the L3 deposits are nearly all well-bonded due to surface diffusion between the less tightly bounded atoms within the surface defects, which is analogous to the sintering process. Recovery and diffusion-driven processes such as recrystallization and spheroidization of planar inter-particle defects also play a crucial role in microstructure evolution resembling the annealing process [55]. In addition to the thermal annealing effect of the laser beam, the constant irradiation on the deposits remarkably decreases the V_{cr} of powders, which benefits from the thermal softening and surface oxidation film removal of substrates and

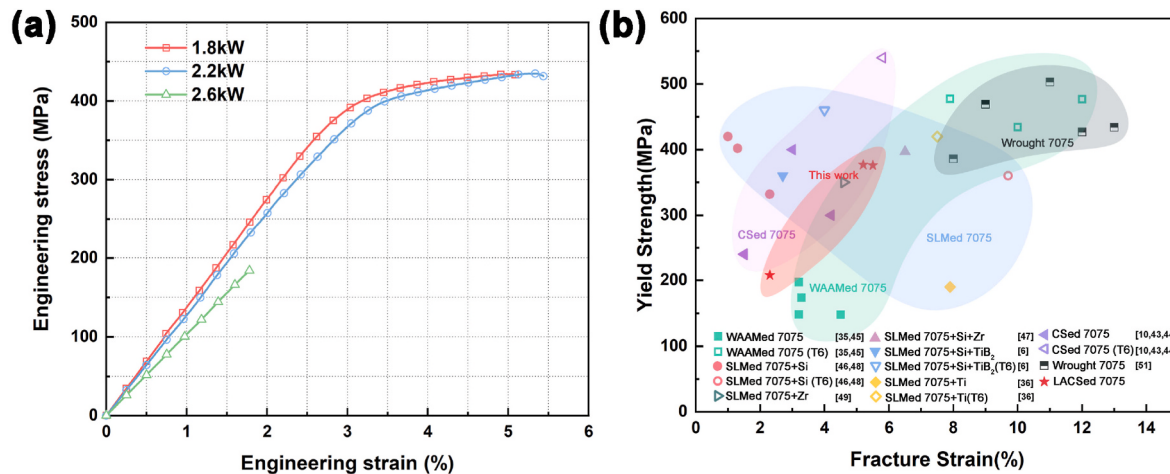


Fig. 12. (a)The engineering stress-strain curve of LACsed deposits, and (b) comparative maps with other AM fabricated 7075 components in mechanic properties.

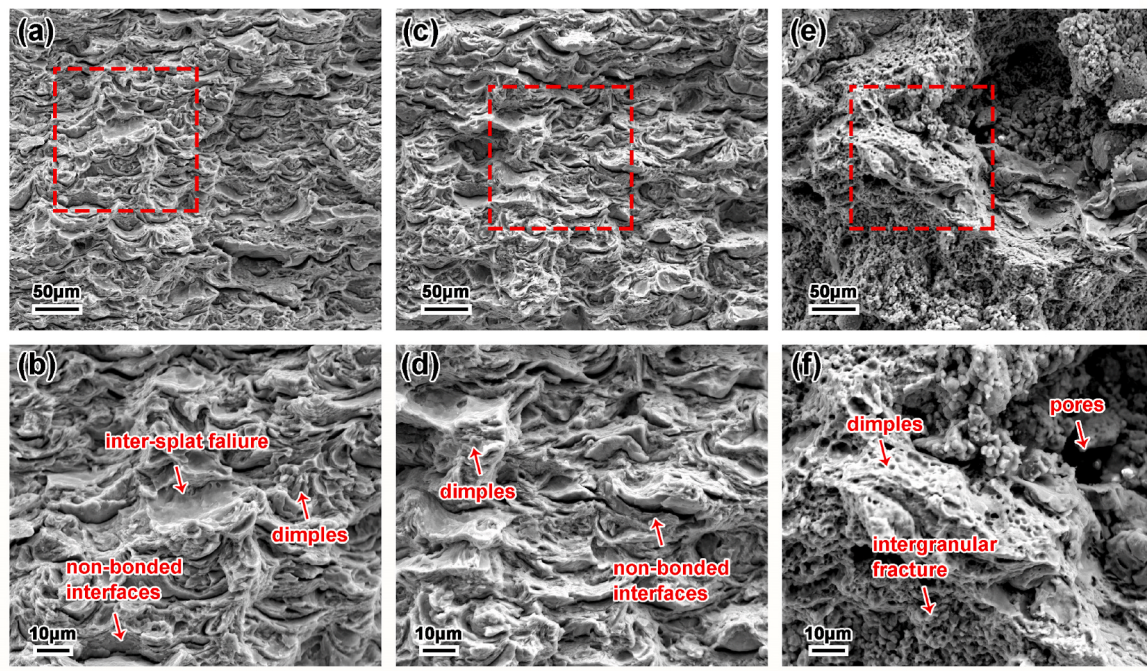


Fig. 13. Fracture morphologies of (a–b) L1 deposits, (c–d) L2 deposits, and (e–f) L3 deposits. Images on the second row are the zoom-in picture of the areas encircled by the red boxes on the left column. (For interpretation of the references to color in this figure legend, the reader is referred to the Web version of this article.)

consequently increases the value of η and improve the overall quality of deposits.

4.1.2. Grain boundary strengthening

One of the most significant microstructure evolutions with the rising laser power is grain growth and recovery under the annealing effect of laser, reducing the density of grain boundaries which act as strong obstacles to dislocation motion and attenuated dislocation interaction induced by multiple slips during the deformation, consequently lowering the strength of deposits to some extent. The grain boundary strengthening is usually described by the empirical Hall-Petch equation [56]:

$$\sigma_y = \sigma_0 + \frac{k_y}{\sqrt{d}} \quad (4)$$

where d is the average grain diameter, σ_0 is the frictional stress required to move dislocations and k_y is the Hall-Petch slope.

Although there is still some controversy regarding the application of the Hall-Petch relationship to the submicrometer scale grains in aluminum alloys produced by severe plastic deformation (SPD), previous investigations confirmed that the Hall-Petch relationship persists down to at least several-hundred-nanometer scale only with a decrease in the slope of the Hall-Petch plot at the very finest grain sizes [57,58]. The k_y was proved to be about $0.12 \text{ MPa}/\sqrt{m}$ for peak-aged Al 7075 [59]. Assuming the value of σ_0 keep constant during the LACS process, thus the strength variation from grain boundary strengthening, $\Delta\sigma_{gb}$ just originated from the changing of d , and it was estimated as 151, 141, 135, and 79 MPa for L0, L1, L2, and L3 deposits, respectively.

4.1.3. Solid solution strengthening

Solid solution hardening is another strengthening mechanism in LACS 7075 deposits as the introduction of solute atoms, including Zn, Mg, and Cu, produces a lattice dilation that typically gives rise to the stress fields around the solute atom and interacts with dislocations. These interactions derived from the size difference or electrical and chemical elastic modulus mismatch between host atoms and solute

atoms all give rise to the energy barrier to dislocation motion. The solid solution hardening is generally described by the Fleischer equation [56]:

$$\Delta\sigma_{ss} = \frac{MG\dot{\varepsilon}_{ss}^{\frac{3}{2}}\sqrt{c}}{700} \quad (5a)$$

$$\dot{\varepsilon}_{ss} = |\dot{\varepsilon}_G - \beta\dot{\varepsilon}_b| \quad (5b)$$

$$\dot{\varepsilon}_G = \frac{\dot{\varepsilon}_G}{1 + \frac{1}{2}|\dot{\varepsilon}_G|} \quad (5c)$$

$$\dot{\varepsilon}_b = \frac{1}{b} \frac{db}{dc} \quad (5d)$$

$$\dot{\varepsilon}_b = \frac{1}{b} \frac{db}{dc} \quad (5e)$$

where M is the mean orientation factor and equals 3.06 for the fcc polycrystalline matrix, G is the shear modulus and the value of 26.9 GPa is adopted for 7075 alloy, b is the Burgers vector and equals 0.286 nm for fcc 7075 alloy, c is the atomic concentration of a solute, β is 3, and a is the lattice parameter of the Al matrix, 0.405 nm. Combined with all these data, the theoretical yield strength increments by main solute elements Al, Zn, and Cu were calculated as 15, 48, and 22 MPa, respectively. The total yield strength increase resulting from the solid strengthening mechanism was calculated as ~ 85 MPa. The value was obtained on the condition that all the solute atoms were uniformly distributed in the Al matrix. Unfortunately, the composition separation and intermetallic spread along the grain boundaries mentioned above implied a lower contribution of solid solution atoms.

4.1.4. Dislocation strengthening

As is known to all, the particles usually are accelerated to supersonic speed in the CS process and subject to severe plastic deformation during the deposition. The plastic deformation and the consequent work-hardening result in an increase in the dislocation density. As discussed above, the heightening of dislocation interaction will eventually increase the yield strength of materials. The contribution of dislocation

strengthening was described as follows [56]:

$$\Delta\sigma_d = M\alpha Gb\rho^{\frac{1}{2}} \quad (6a)$$

$$\rho = \frac{2\sqrt{3}\epsilon}{db} \quad (6b)$$

where α is a constant and equals 0.2 for fcc metals, ρ is the dislocation density b is the Burgers vector, d , and ϵ is the crystallite diameter that we calculated in section 2. The dislocation density was finally calculated as 3.5×10^{14} , 2.1×10^{14} , 2.1×10^{14} , and $1.8 \times 10^{14} \text{ m}^{-2}$ for L0, L1, L2, and L3 deposits, respectively. $\Delta\sigma_d$ is therefore 88, 68, 68, and 64 MPa for each deposit.

4.1.5. Precipitation strengthening

7075 alloy, one of the age-hardenable aluminum alloys, usually exploits precipitation hardening as the main strengthening technique. The degree of strengthening depends on several factors, including particle size, volume fraction, particle shape, and the nature of the boundary between the particle and the matrix. According to the XRD and SEM results, the T phase, η phase, and intermetallic phase $\text{Al}_7\text{Cu}_2\text{Fe}$ are probably present in the LACSeD 7075 deposits. Unfortunately, more detailed characterization by TEM or APT on these nanoscale dispersoids is needed to make a quantitative description of the degree of precipitation strengthening. The yield strength of the LACSeD 7075 alloy σ_y is composed with:

$$\sigma_y = \sigma_0 + \Delta\sigma_{gb} + \Delta\sigma_{ss} + \Delta\sigma_d + \Delta\sigma_{ps} \quad (7)$$

where σ_0 is estimated at 49 MPa for Al-3.5%Mg alloy [60]. For the LACSeD L1 and L2 deposits, the $\Delta\sigma_{ps}$ could be respectively calculated as 33 MPa and 40 MPa if we take the upper limit of $\Delta\sigma_{ss}$. In reality, the exact value of $\Delta\sigma_{ps}$ could be higher as the compensation of precipitation of solute atoms to the second phase, but it doesn't impede grain boundary strengthening to be the predominant mechanism in the L1 and L2 deposits. In the L0 and L3 deposits, the sum of calculated yield strength without $\Delta\sigma_{ps}$ is 324 MPa and 228 MPa, respectively, which is in excess of the measured values from the experiment, indicating a defect-control fracture mode in the two deposits.

4.2. Pores formation mechanism

As we have discussed above, the anomalous increases in porosity in the LACSeD L3 deposits degraded its mechanical properties and inhibited the extensive application of this solid-state AM technology. The pores formation in Al alloys made by fusion-based AM technology is usually driven by a variety of factors, including partial melting, shrinkage, gas entrapment, and so forth [61]. However, the origin mechanisms of the pores in the CS and LACS processes are somewhat different. The pores and detachments probably resulted from the low impact velocity of 7075 particles at this specific gas condition, in which the particles have a higher likelihood of rebounding than of attaching to the substrate. Pores in CSed materials are typically brought on by inadequate plastic deformation of particles, which commonly appear at the intersection of numerous particles. When particles with broad size distribution are deposited with CS, large and small cavities are generated resulting from particle bridging and interparticle gap respectively.

The pore formation mechanism in the LACSeD deposits becomes more intricate and varied with the change of laser power. The L0 and L1 deposits presented comparable pore morphologies, indicating the similar pores formation mechanism in these two deposits. The L2 deposits exhibited lower porosity by virtue of sufficient plastic deformation of particles as shown in Fig. 3. However, a mass of small spherical pores was found widespread at grains and particles' boundaries when the laser power increased to 2.6 kW in Fig. 14. As laser power increased, the heat-softening impact of the laser on the substrate and particles began to play a more significant role in the LACS process. The critical

velocity would decrease as particle and substrate temperatures rose. As a result, the decreased porosity in the L2 deposits is predictable. However, strong oxidation also formed at the particle interface as a result of the high laser intensity impeding efficient particle bonding in the LACSeD deposits. Fig. 14 confirmed that several tiny holes at the prior-particle interface were significantly enriched in the elements O and Mg. The oxide layers covering the particle surface severely hindered the bonding between particles and the tiny pores usually generated between them. The overall surface energy was finally decreased by the convergence of these tiny holes into big pores of various sizes. The converging phenomenon of tiny pores had been observed in the vacuum heat treatment of Ti and Ti-6Al-4V CSed coatings, as well as the solution heat treatment of Al-Si-Mg alloys [62,63].

5. Conclusions

This study is an initial look into the LACS of 7075 alloy. The following conclusions were drawn from the experiment:

- i. Laser-assisted cold spray of 7075 alloy produced fully consolidated deposits with a tightly bounded substrate-deposit interface at a median laser power of 2.2 kW. The deposition thickness and porosity exhibited a virtually linear increase and U-shape change respectively as the laser power increased. Compared with SLS and WAAM, defects like hot cracks and texture were avoided in deposits due to the absence of the solidification process in LACS.
- ii. The evolution of microstructure was examined with increased laser power. The T phase ($\text{Al}_2\text{Mg}_3\text{Zn}_3$) in as-received powder remained until laser power was below 2.2 kW. Large amounts of lamellar η phase $\text{Mg}(\text{Zn}, \text{Cu}, \text{Al})_2$ and $\text{Al}_7\text{Cu}_2\text{Fe}$ precipitated along grain boundaries at the highest laser power of 2.6 kW. Recrystallization occurred in the 7075 deposits and nearly equiaxed grain morphology was eventually obtained. Significant grain growth was also observed under the influence of in-situ laser heat treatment.
- iii. Adhesion strength was measured at more than 50 MPa for all the LACSeD deposits, which is well above the CSed one. The CSed deposit exhibited the highest average hardness of 143 Hv due to the work-hardening effect. Microstructure of LACSeD deposits, such as grain size, porosity, and precipitation showed a combined effect on its hardness.
- iv. The tensile property exhibited significant growth for the LACSeD 7075 deposits. The yield strength and EL to fracture for L1, L2 and L3 deposits were 376 MPa, 377 MPa, 208 MPa and 5.4%, 5.2%, 2.8%, respectively. The strengthening in LACSeD 7075 deposits was probably owing to the elimination of macroscopic defects and grain boundary strengthening.
- v. The mechanism of pore formation changed with laser power. The pores in CSed deposits were mainly induced by insufficient deformation between particles. As the laser power increased, tiny pores resulting from strong oxidation converged into large and irregular pores in recrystallized grain areas eventually.

CRediT author statement

Kang Wang: Conceptualization, Methodology, Investigation, Writing - Original Draft. Lijia Zhao: Investigation. Tianliang Mao: Investigation. Jiqiang Wang: Conceptualization, Methodology, Resources, Writing - Review & Editing, Supervision, Funding acquisition. Tianying Xiong: Supervision, Project administration. Xinyu Cui: Supervision, Project administration.

Declaration of competing interest

The authors declare that they have no known competing financial interests or personal relationships that could have appeared to influence

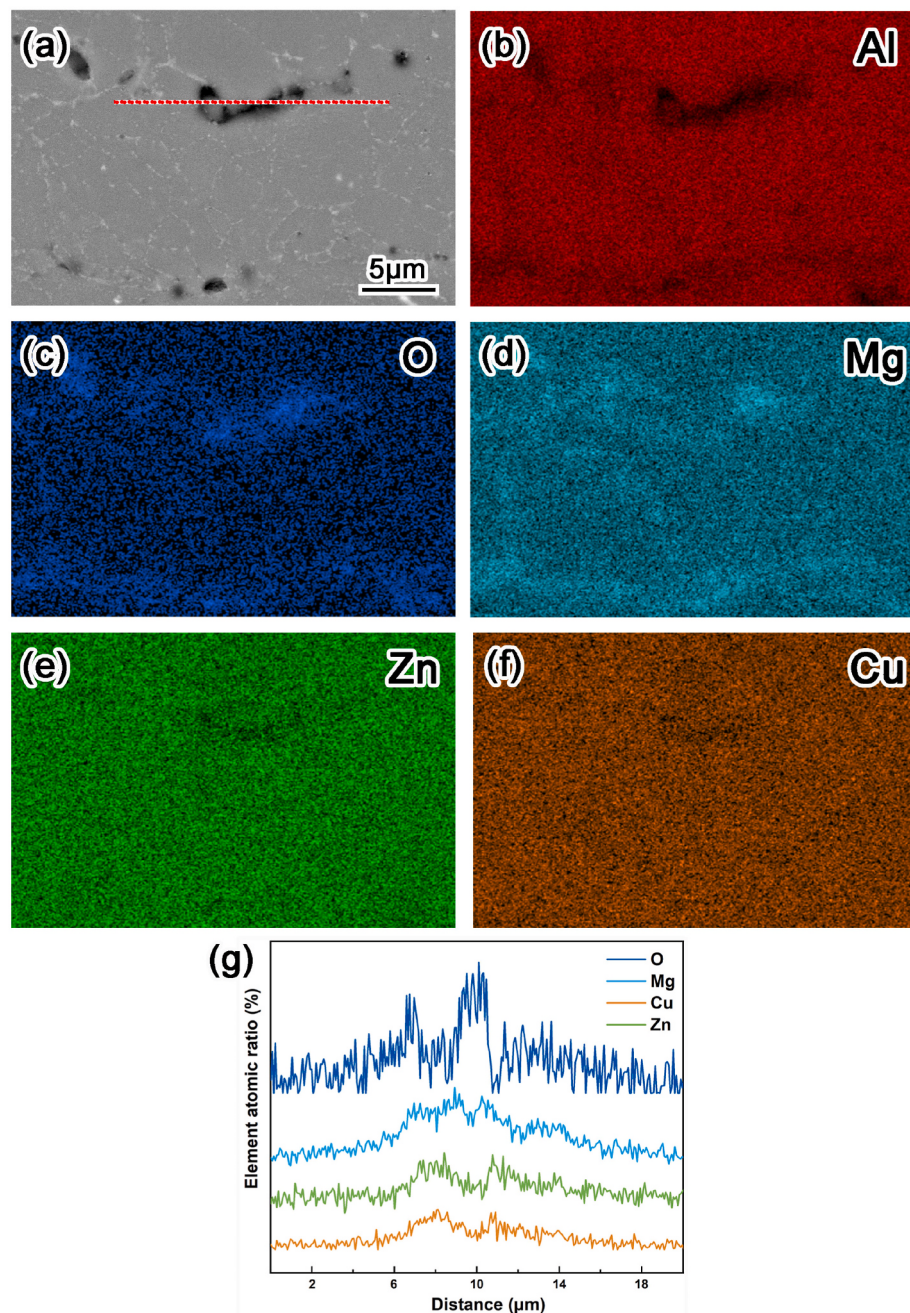


Fig. 14. EDS mapping of LACsed L3 deposits showing the oxidation around the small pores distributed in grain boundaries.

the work reported in this paper.

Data availability

Data will be made available on request.

Acknowledgment

The financial support of the Natural Science Foundation of Liaoning Province, China (Grant No. 2021-MS-002) is gratefully acknowledged.

References

- [1] T. Dursun, C. Soutis, Recent developments in advanced aircraft aluminum alloys, *Mater. Des.* 56 (2014) 862–871, <https://doi.org/10.1016/j.matdes.2013.12.002>.
- [2] B. Blakey-Milner, P. Gradi, G. Snedden, M. Brooks, J. Pitot, E. Lopez, M. Leary, F. Berto, A. du Plessis, Metal additive manufacturing in aerospace: a review, *Mater. Des.* 209 (2021), <https://doi.org/10.1016/j.matdes.2021.110008>.
- [3] T. Yuan, Z. Yu, S. Chen, M. Xu, X. Jiang, Loss of elemental Mg during wire + arc additive manufacturing of Al-Mg alloy and its effect on mechanical properties, *J. Manuf. Process.* 49 (2020) 456–462, <https://doi.org/10.1016/j.jmapro.2019.10.033>.
- [4] D. Liu, D. Wu, R. Wang, J. Shi, F. Niu, G. Ma, Formation mechanism of Al-Zn-Mg-Cu alloy fabricated by laser-arc hybrid additive manufacturing: microstructure evaluation and mechanical properties, *Addit. Manuf.* 50 (2022), <https://doi.org/10.1016/j.addma.2021.102554>.
- [5] N. Kaufmann, M. Imran, T.M. Wischeropp, C. Emmelmann, S. Siddique, F. Walther, Influence of process parameters on the quality of aluminium alloy EN AW 7075 using selective laser melting (SLM), *Phys. Procedia* 83 (2016) 918–926, <https://doi.org/10.1016/j.phpro.2016.08.096>.
- [6] S.Y. Zhou, Y. Su, H. Wang, J. Enz, T. Ebel, M. Yan, Selective laser melting additive manufacturing of 7xxx series Al-Zn-Mg-Cu alloy: cracking elimination by co-incorporation of Si and TiB₂, *Addit. Manuf.* 36 (2020), <https://doi.org/10.1016/j.addma.2020.101458>.

- [7] J.H. Martin, B.D. Yahata, J.M. Hundley, J.A. Mayer, T.A. Schaedler, T.M. Pollock, 3D printing of high-strength aluminium alloys, *Nature* 549 (7672) (2017) 365–369, <https://doi.org/10.1038/nature23894>.
- [8] W. Li, K. Yang, S. Yin, X. Yang, Y. Xu, R. Lupoi, Solid-state additive manufacturing and repairing by cold spraying: a review, *J. Mater. Sci. Technol.* 34 (3) (2018) 440–457, <https://doi.org/10.1016/j.jmst.2017.09.015>.
- [9] H. Assadi, H. Kreye, F. Gärtner, T. Klassen, Cold spraying – a materials perspective, *Acta Mater.* 116 (2016) 382–407, <https://doi.org/10.1016/j.actamat.2016.06.034>.
- [10] Y. Ren, N.U.H. Tariq, H. Liu, L. Zhao, X. Cui, Y. Shen, J. Wang, T. Xiong, Study of microstructural and mechanical anisotropy of 7075 Al deposits fabricated by cold spray additive manufacturing, *Mater. Des.* 212 (2021), <https://doi.org/10.1016/j.matdes.2021.110271>.
- [11] M. Bray, A. Cockburn, W. O'Neill, The Laser-assisted Cold Spray process and deposit characterisation, *Surf. Coatings. Technol.* 203 (19) (2009) 2851–2857, <https://doi.org/10.1016/j.surfcoat.2009.02.135>.
- [12] E.O. Olakanmi, M. Doyoyo, Laser-assisted cold-sprayed corrosion- and wear-resistant coatings: a review, *J. Therm. Spray Technol.* 23 (5) (2014) 765–785, <https://doi.org/10.1007/s11666-014-0098-x>.
- [13] M. Jones, A. Cockburn, R. Lupoi, M. Sparkes, W. O'Neill, Solid-state manufacturing of tungsten deposits onto molybdenum substrates with supersonic laser deposition, *Mater. Lett.* 134 (2014) 295–297, <https://doi.org/10.1016/j.matlet.2014.07.091>.
- [14] J. Yao, L. Yang, B. Li, Z. Li, Characteristics and performance of hard Ni60 alloy coating produced with supersonic laser deposition technique, *Mater. Des.* 83 (2015) 26–35, <https://doi.org/10.1016/j.matdes.2015.05.087>.
- [15] F. Luo, A. Cockburn, R. Lupoi, M. Sparkes, W. O'Neill, Performance comparison of Stellite 6® deposited on steel using supersonic laser deposition and laser cladding, *Surf. Coatings. Technol.* 212 (2012) 119–127, <https://doi.org/10.1016/j.surfcoat.2012.09.031>.
- [16] J. Yao, Z. Li, B. Li, L. Yang, Characteristics and bonding behavior of Stellite 6 alloy coating processed with supersonic laser deposition, *J. Alloys Compd.* 661 (2016) 526–534, <https://doi.org/10.1016/j.jallcom.2015.11.077>.
- [17] B. Li, Y. Jin, J. Yao, Z. Li, Q. Zhang, X. Zhang, Influence of laser irradiation on deposition characteristics of cold sprayed Stellite-6 coatings, *Opt. Laser Technol.* 100 (2018) 27–39, <https://doi.org/10.1016/j.optlastec.2017.09.034>.
- [18] B. Li, J. Yao, Q. Zhang, Z. Li, L. Yang, Microstructure and tribological performance of tungsten carbide reinforced stainless steel composite coatings by supersonic laser deposition, *Surf. Coatings Technol.* 275 (2015) 58–68, <https://doi.org/10.1016/j.surfcoat.2015.05.040>.
- [19] J. Yao, L. Yang, B. Li, Z. Li, Beneficial effects of laser irradiation on the deposition process of diamond/Ni60 composite coating with cold spray, *Appl. Surf. Sci.* 330 (2015) 300–308, <https://doi.org/10.1016/j.apsusc.2015.01.029>.
- [20] B. Li, Y. Jin, J. Yao, Z. Li, Q. Zhang, Solid-state fabrication of WCp-reinforced Stellite-6 composite coatings with supersonic laser deposition, *Surf. Coatings Technol.* 321 (2017) 386–396, <https://doi.org/10.1016/j.surfcoat.2017.04.062>.
- [21] L. Wu, G. Zhang, B. Li, W. Wang, X. Huang, Z. Chen, G. Dong, Q. Zhang, J. Yao, Study on microstructure and tribological performance of diamond/Cu composite coating via supersonic laser deposition, *Coatings* 10 (3) (2020), <https://doi.org/10.3390/coatings10030276>.
- [22] A.M. Birt, V.K. Champagne, R.D. Sisson, D. Apelian, Statistically guided development of laser-assisted cold spray for microstructural control of Ti-6Al-4V, *Metall. Mater. Trans. A* 48 (4) (2017) 1931–1943, <https://doi.org/10.1007/s11661-017-3970-8>.
- [23] E.O. Olakanmi, M. Tlotteng, C. Meacock, S. Pityana, M. Doyoyo, Deposition mechanism and microstructure of laser-assisted cold-sprayed (LACS) Al-12 wt.%Si coatings: effects of laser power, *JOM* 65 (6) (2013) 776–783, <https://doi.org/10.1007/s11837-013-0611-6>.
- [24] E.O. Olakanmi, Optimization of the quality characteristics of laser-assisted cold-sprayed (LACS) aluminum coatings with Taguchi design of experiments (DOE), *Mater. Manuf. Process.* 31 (11) (2015) 1490–1499, <https://doi.org/10.1080/10426914.2014.984306>.
- [25] G.K. Williamson, W.H. Hall, X-ray line broadening from filed aluminum and wolfram, *Acta Metall.* 1 (1) (1953) 22–31, [https://doi.org/10.1016/0001-6160\(53\)90006-6](https://doi.org/10.1016/0001-6160(53)90006-6).
- [26] M.R. Rokni, C.A. Widener, G.A. Crawford, Microstructural evolution of 7075 Al gas atomized powder and high-pressure cold sprayed deposition, *Surf. Coatings. Technol.* 251 (2014) 254–263, <https://doi.org/10.1016/j.surfcoat.2014.04.035>.
- [27] A. Sabard, P. McNutt, H. Begg, T. Hussain, Cold spray deposition of solution heat treated, artificially aged and naturally aged Al 7075 powder, *Surf. Coatings. Technol.* 385 (2020), <https://doi.org/10.1016/j.surfcoat.2020.125367>.
- [28] Y. Liu, D. Jiang, W. Xie, J. Hu, B. Ma, Solidification phases and their evolution during homogenization of a DC cast Al-8.35Zn-2.5Mg-2.25Cu alloy, *Mater. Charact.* 93 (2014) 173–183, <https://doi.org/10.1016/j.matchar.2014.04.004>.
- [29] D. Xu, Z. Li, G. Wang, X. Li, X. Lv, Y.a. Zhang, Y. Fan, B. Xiong, Phase transformation and microstructure evolution of an ultra-high strength Al-Zn-Mg-Cu alloy during homogenization, *Mater. Charact.* 131 (2017) 285–297, <https://doi.org/10.1016/j.matchar.2017.07.011>.
- [30] X.-l. Zou, H. Yan, X.-h. Chen, Evolution of second phases and mechanical properties of 7075 Al alloy processed by solution heat treatment, *Trans. Nonferrous Metals Soc. China* 27 (10) (2017) 2146–2155, [https://doi.org/10.1016/s1003-6326\(17\)60240-1](https://doi.org/10.1016/s1003-6326(17)60240-1).
- [31] M.A. Jabbari Taleghani, E.M. Ruiz Navas, J.M. Torralba, Microstructural and mechanical characterisation of 7075 aluminium alloy consolidated from a premixed powder by cold compaction and hot extrusion, *Mater. Des.* 55 (2014) 674–682, <https://doi.org/10.1016/j.matdes.2013.10.028>.
- [32] W. Yuan, J. Zhang, C. Zhang, Z. Chen, Processing of ultra-high strength SiCp/Al-Zn-Mg-Cu composites, *J. Mater. Process. Technol.* 209 (7) (2009) 3251–3255, <https://doi.org/10.1016/j.jmatprotec.2008.07.030>.
- [33] M.M. Tünçay, J.A. Muñiz-Lerma, D.P. Bishop, M. Brochu, Spark plasma sintering and upsetting of a gas-atomized/air-atomized Al alloy powder mixture, *J. Mater. Eng. Perform.* 26 (10) (2017) 5097–5106, <https://doi.org/10.1007/s11665-017-2948-4>.
- [34] P. Wang, H.C. Li, K.G. Prashanth, J. Eckert, S. Scudino, Selective laser melting of Al-Zn-Mg-Cu: heat treatment, microstructure and mechanical properties, *J. Alloys Compd.* 707 (2017) 287–290, <https://doi.org/10.1016/j.jallcom.2016.11.210>.
- [35] B. Dong, X. Cai, S. Lin, X. Li, C. Fan, C. Yang, H. Sun, Wire arc additive manufacturing of Al-Zn-Mg-Cu alloy: microstructures and mechanical properties, *Addit. Manuf.* 36 (2020), <https://doi.org/10.1016/j.addma.2020.101447>.
- [36] Q. Tan, Z. Fan, X. Tang, Y. Yin, G. Li, D. Huang, J. Zhang, Y. Liu, F. Wang, T. Wu, X. Yang, H. Huang, Q. Zhu, M.-X. Zhang, A novel strategy to additively manufacture 7075 aluminium alloy with selective laser melting, *Mater. Sci. Eng., A* 821 (2021), <https://doi.org/10.1016/j.msea.2021.141638>.
- [37] Q. Wang, N. Birbilis, H. Huang, M.-X. Zhang, Microstructure characterization and nanomechanics of cold-sprayed pure Al and Al-Al2O3 composite coatings, *Surf. Coatings Technol.* 232 (2013) 216–223, <https://doi.org/10.1016/j.surfcoat.2013.05.009>.
- [38] X.-T. Luo, C.-X. Li, F.-L. Shang, G.-J. Yang, Y.-Y. Wang, C.-J. Li, High velocity impact induced microstructure evolution during deposition of cold spray coatings: a review, *Surf. Coatings Technol.* 254 (2014) 11–20, <https://doi.org/10.1016/j.surfcoat.2014.06.006>.
- [39] Y. Xie, S. Yin, J. Cizek, J. Cupera, E. Guo, R. Lupoi, Formation mechanism and microstructure characterization of nickel-aluminum intertwining interface in cold spray, *Surf. Coatings Technol.* 337 (2018) 447–452, <https://doi.org/10.1016/j.surfcoat.2018.01.049>.
- [40] K. Huang, R.E. Logé, A review of dynamic recrystallization phenomena in metallic materials, *Mater. Des.* 111 (2016) 548–574, <https://doi.org/10.1016/j.matdes.2016.09.012>.
- [41] N. Allain-Bonasso, F. Wagner, S. Berbenni, D.P. Field, A study of the heterogeneity of plastic deformation in IF steel by EBSD, *Mater. Sci. Eng., A* 548 (2012) 56–63, <https://doi.org/10.1016/j.msea.2012.03.068>.
- [42] A.J. Schwartz, M. Kumar, B.L. Adams, D.P. Field, *Electron Backscatter Diffraction in Materials Science*, Springer, US, 2009.
- [43] X. Xie, Y. Ma, C. Chen, G. Ji, C. Verdy, H. Wu, Z. Chen, S. Yuan, B. Normand, S. Yin, H. Liao, Cold spray additive manufacturing of metal matrix composites (MMCs) using a novel nano-TiB2-reinforced 7075Al powder, *J. Alloys Compd.* 819 (2020), <https://doi.org/10.1016/j.jallcom.2019.152962>.
- [44] M.R. Rokni, C.A. Widener, V.K. Champagne, G.A. Crawford, S.R. Nutt, The effects of heat treatment on 7075 Al cold spray deposits, *Surf. Coatings Technol.* 310 (2017) 278–285, <https://doi.org/10.1016/j.surfcoat.2016.10.064>.
- [45] T. Klein, M. Schnall, B. Gomes, P. Warczok, D. Fleischhacker, P.J. Morais, Wire-arc additive manufacturing of a novel high-performance Al-Zn-Mg-Cu alloy: processing, characterization and feasibility demonstration, *Addit. Manuf.* 37 (2021), <https://doi.org/10.1016/j.addma.2020.101663>.
- [46] R. Casati, M. Coduri, M. Ruccio, A. Rizzi, M. Vedani, Development of a high strength Al-Zn-Si-Mg-Cu alloy for selective laser melting, *J. Alloys Compd.* 801 (2019) 243–253, <https://doi.org/10.1016/j.jallcom.2019.06.123>.
- [47] L. Li, R. Li, T. Yuan, C. Chen, Z. Zhang, X. Li, Microstructures and tensile properties of a selective laser melted Al-Zn-Mg-Cu (Al7075) alloy by Si and Zr microalloying, *Mater. Sci. Eng., A* 787 (2020), <https://doi.org/10.1016/j.msea.2020.139492>.
- [48] Y. Otani, S. Sasaki, Effects of the addition of silicon to 7075 aluminum alloy on microstructure, mechanical properties, and selective laser melting processability, *Mater. Sci. Eng., A* 777 (2020), <https://doi.org/10.1016/j.msea.2020.139079>.
- [49] H. Zhang, H. Zhu, X. Nie, J. Yin, Z. Hu, X. Zeng, Effect of Zirconium addition on crack, microstructure and mechanical behavior of selective laser melted Al-Cu-Mg alloy, *Scr. Mater.* 134 (2017) 6–10, <https://doi.org/10.1016/j.scriptamat.2017.02.036>.
- [50] Q. Tan, J. Zhang, Q. Sun, Z. Fan, G. Li, Y. Yin, Y. Liu, M.-X. Zhang, Inoculation treatment of an additively manufactured 2024 aluminium alloy with titanium nanoparticles, *Acta Mater.* 196 (2020) 1–16, <https://doi.org/10.1016/j.jactamat.2020.06.026>.
- [51] J. Davis, *ASM Specialty Handbook: Aluminum and Aluminum Alloys*, 1993.
- [52] M.V. Vidaller, A. List, F. Gaertner, T. Klassen, S. Dosta, J.M. Guilemany, Single impact bonding of cold sprayed Ti-6Al-4V powders on different substrates, *J. Therm. Spray Technol.* 24 (4) (2015) 644–658, <https://doi.org/10.1007/s11666-014-0200-4>.
- [53] H. Assadi, *Application of Analytical methods for understanding and optimization of the cold spray process*, 2003, in: *Proc. of 6th HVOF Colloquium*, 2003.
- [54] H. Assadi, T. Schmidt, H. Richter, J.O. Kliemann, K. Binder, F. Gaertner, T. Klassen, H. Kreye, On parameter selection in cold spraying, *J. Therm. Spray Technol.* 20 (6) (2011) 1161–1176, <https://doi.org/10.1007/s11666-011-9662-9>.
- [55] C. Huang, M. Arseenko, L. Zhao, Y. Xie, A. Elsener, W. Li, F. Gaertner, A. Simar, T. Klassen, Property prediction and crack growth behavior in cold sprayed Cu deposits, *Mater. Des.* 206 (2021), <https://doi.org/10.1016/j.matdes.2021.109826>.
- [56] T.H. Courtney, *Mechanical Behaviour of Materials*, second ed., 2005.
- [57] M. Furukawa, Z. Horita, M. Nemoto, R.Z. Valiev, T.G. Langdon, Microhardness measurements and the Hall-Petch relationship in an Al-Mg alloy with submicrometer grain size, *Acta Mater.* 44 (11) (1996) 4619–4629, [https://doi.org/10.1016/1359-6454\(96\)00105-x](https://doi.org/10.1016/1359-6454(96)00105-x).
- [58] Z. Horita, T. Fujinami, M. Nemoto, T.G. Langdon, Improvement of mechanical properties for Al alloys using equal-channel angular pressing, *J. Mater. Process.*

- Technol. 117 (3) (2001) 288–292, [https://doi.org/10.1016/s0924-0136\(01\)00783-x](https://doi.org/10.1016/s0924-0136(01)00783-x).
- [59] K. Ma, H. Wen, T. Hu, T.D. Topping, D. Isheim, D.N. Seidman, E.J. Lavernia, J. M. Schoenung, Mechanical behavior and strengthening mechanisms in ultrafine grain precipitation-strengthened aluminum alloy, *Acta Mater.* 62 (2014) 141–155, <https://doi.org/10.1016/j.actamat.2013.09.042>.
- [60] M.A. Meyers, K.K. Chawla, *Mechanical Behavior of Materials*, Cambridge University Press, 2008.
- [61] E.O. Olakanmi, R.F. Cochrane, K.W. Dalgarno, A review on selective laser sintering/melting (SLS/SLM) of aluminium alloy powders: processing, microstructure, and properties, *Prog. Mater. Sci.* 74 (2015) 401–477, <https://doi.org/10.1016/j.pmatsci.2015.03.002>.
- [62] W.Y. Li, C. Zhang, X. Guo, J. Xu, C.J. Li, H. Liao, C. Coddet, K.A. Khor, Ti and Ti-6Al-4V coatings by cold spraying and microstructure modification by heat treatment, *Adv. Eng. Mater.* 9 (5) (2007) 418–423, <https://doi.org/10.1002/adem.200700022>.
- [63] K.V. Yang, P. Rometsch, T. Jarvis, J. Rao, S. Cao, C. Davies, X. Wu, Porosity formation mechanisms and fatigue response in Al-Si-Mg alloys made by selective laser melting, *Mater. Sci. Eng., A* 712 (2018) 166–174, <https://doi.org/10.1016/j.msea.2017.11.078>.